Scanning ARM Cloud Radars. Part II: Data Quality Control and Processing

PAVLOS KOLLIAS, IENG JO, PALOMA BORQUE, ALEKSANDRA TATAREVIC, AND KATIA LAMER

Department of Atmospheric and Oceanic Sciences, McGill University, Montreal, Quebec, Canada

NITIN BHARADWAJ AND KEVIN WIDENER

Pacific Northwest National Laboratory, Richland, Washington

KAREN JOHNSON

Brookhaven National Laboratory, Upton, New York

EUGENE E. CLOTHIAUX

Department of Meteorology, The Pennsylvania State University, State College, Pennsylvania

(Manuscript received 12 February 2013, in final form 4 October 2013)

ABSTRACT

The scanning Atmospheric Radiation Measurement (ARM) Program cloud radars (SACRs) are the primary instruments for documenting the four-dimensional structure and evolution of clouds within a 20–30-km radius of the ARM fixed and mobile sites. Here, the postprocessing of the calibrated SACR measurements is discussed. First, a feature mask algorithm that objectively determines the presence of significant radar returns is described. The feature mask algorithm is based on the statistical properties of radar receiver noise. It accounts for atmospheric emission and is applicable even for SACR profiles with few or no signal-free range gates. Using the nearest-in-time atmospheric sounding, the SACR radar reflectivities are corrected for gaseous attenuation (water vapor and oxygen) using a line-by-line absorption model. Despite having a high pulse repetition frequency, the SACR has a narrow Nyquist velocity limit and thus Doppler velocity folding is commonly observed. An unfolding algorithm that makes use of a first guess for the true Doppler velocity using horizontal wind measurements from the nearest sounding is described. The retrieval of the horizontal wind profile from the hemispherical sky range–height indicator SACR scan observations and/or nearest sounding is described. The retrieved horizontal wind profile can be used to adaptively configure SACR scan strategies that depend on wind direction. Several remaining challenges are discussed, including the removal of insect and second-trip echoes. The described algorithms significantly enhance SACR data quality and constitute an important step toward the utilization of SACR measurements for cloud research.

1. Introduction

The U.S. Department of Energy Atmospheric Radiation Measurement (ARM) Program operates scanning ARM cloud radars (SACRs) at all its fixed and mobile sites (Kollias et al. 2014). The acquisition and operation of these state-of-the-art systems constitutes the first network of continuously operating scanning cloud radars and is expected to address several observational shortcomings of ARM's profiling cloud radars (Kollias et al. 2014). Much of the future impact these systems will have on cloud and precipitation research depends on how they are used to sample the atmosphere to capture the three-dimensional structure of clouds and their temporal evolution. While a first set of generic scan strategies has been implemented (Kollias et al. 2014), it is adaptable and changes will be made to it as necessary in support of future cloud studies. Another important step in the full utilization of the SACR observations for cloud and precipitation research is the development of quality-controlled data products.

The transition from the one-dimensional ''soda straw'' view of the atmosphere to a three-dimensional view over

Corresponding author address: Pavlos Kollias, Department of Atmospheric and Oceanic Sciences, Room 945, Burnside Hall, 805 Sherbrooke Street West, Montreal QC H3A 0B9, Canada.
E-mail: pavlos.kollias@mcgill.ca

DOI: 10.1175/JTECH-D-13-00045.1

a large domain creates several challenges that must be tackled in order for the new observations to be useful and relevant to modelers. Challenges similar to those faced during the first days of ARM will need to be revisited: How is a cloudy atmosphere best sampled in three dimensions? What are the critical measurements or parameters that must be obtained? How should the data from the different remote sensors be packaged and gridded? It took several years for ARM to address these issues in one dimension and the same will probably be true of three dimensions. Past ARM efforts led to the development of new instruments, new sampling strategies, and the design of several new synergetic algorithms. To date, the most widely used ARM product from the ARM profiling millimeter-wavelength radars (Moran et al. 1998; Kollias et al. 2007) has been the active remote sensing of clouds (ARSCL) product (Clothiaux et al. 2000).

The ARSCL hydrometeor detection algorithm uses a binary cloud mask (Clothiaux et al. 1995) from the profiling cloud radar, the micropulse lidar detection mask, and the time series of cloud-base heights from the ceilometer to extract the hydrometeor locations in the atmospheric column. The laser measurements complement the radar observations, especially in the case of tenuous clouds in the boundary layer and upper troposphere. Such complementary measurements are not available in three dimensions; thus, objective determination of hydrometeor locations in SACR data must be based on SACR-only measurements. Increased gaseous signal attenuation at millimeter wavelengths can be significant at low elevation angles and needs to be accounted for in the SACR value-added product (VAP). Doppler velocity aliasing is another source of errors in SACR observations. Despite the use of a relatively high pulse repetition frequency (PRF), the short wavelengths of the SACR result in narrow Nyquist velocity boundaries. As a result the horizontal wind projection on the radial Doppler velocity can lead to multiple velocity folding occurrences.

In what follows we outline the steps that must be successfully taken to extract meaningful products from SACR measurements. First, the estimation of the SACR feature mask (FM) is described. The FM is based on the adaptive determination of the SACR noise floor at each elevation and the use of signal coherency in space (Clothiaux et al. 1995). The mask is used to identify cloud boundaries. Next, a procedure for correcting SACR reflectivity measurements for gaseous attenuation is presented. Third, a method for unfolding SACR Doppler velocities using horizontal winds from the nearest-in-time sounding and estimation of a first guess for velocity folding based on the projection of the horizontal winds onto the radial SACR Doppler velocity is presented. Finally, methods for removing insect and second-trip echo contamination of the Doppler spectra are considered.

In addition to these processing steps necessary to extract high-quality moments from SACR measurements, one higher-order method of retrieval is discussed: the generation of in-cloud horizontal wind profiles using the routine climatological hemispherical sky (HS) range–height indicator (RHI) observations. This product provides unique, continuous measurements of in-cloud horizontal winds and precipitation that complement the vertical velocity measurements from the profiling cloud radars at the ARM fixed and mobile sites.

2. Processing of raw calibrated SACR observations

As just discussed, extraction of meaningful moments from raw calibrated SACR observations requires a number of processing steps. We now consider each of these steps in detail.

a. FM algorithm

The FM algorithm identifies the SACR range gates that contain atmospheric returns. This includes returns from insects in the boundary layer, ground-clutter echoes, and second-trip echoes. An example of a SACR raw radar reflectivity field collected during a Hemispherical Sky–Range-Height Indicator (HS-RHI) horizon-to-horizon scan is shown in Fig. 1a. Clouds are observed at multiple altitudes. While the SACR is capable of mapping the cirrus clouds across 40 km, the detection of shallow cumuli is limited to the nearest 5–10 km, due to the drop in SACR sensitivity with range (visible in the radar reflectivity field as an increase with range in reflectivity of the background noise). In addition to meteorological targets, radar artifacts are also present in the image—in this case, resulting from second-trip echoes. Because of its dependency on range, the SACR reflectivity field is not suitable for determining the FM. Thus, the input to the FM algorithm is the radar-received power $P_{\mathrm{rx}}(\theta, \varphi, r)$ in decibels, where θ is the positioner elevation, φ is the positioner azimuth, and r is range. The $P_{\mathrm{rx}}(\theta, \varphi, r)$ field corresponding to Fig. 1a is illustrated in Fig. 1b.

Implementation of the FM algorithm is a two-step process. First, each SACR elevation angle θ (0°–180°) is treated separately. At each θ, the SACR profile consists of a large number N (e.g., 512) of range gates that can be used in statistical tests to objectively provide an estimate of the SACR receiver noise power $P_n(\theta)$. Determination of $P_n(\theta)$ is accomplished using the Hildebrand and Sekhon (1974, hereafter HS74) technique. Although the HS74 objective noise estimation technique was originally developed to identify the noise level in radar

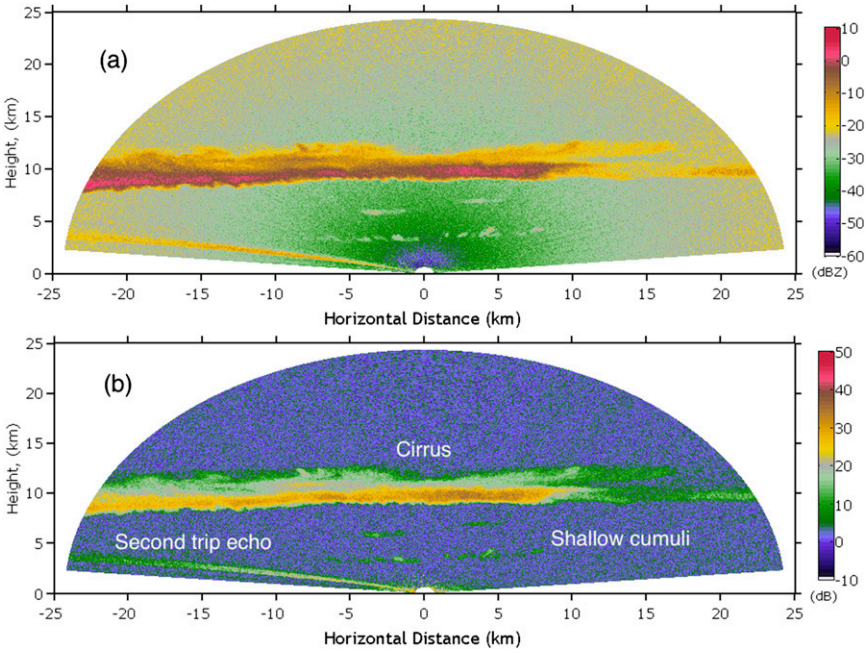

FIG. 1. Example of Ka-band SACR observations from a horizon-to-horizon RHI scan during the Two-Column Aerosol Project (TCAP) at Cape Cod, MA: (a) radar reflectivity and (b) received power (dB).

Doppler spectra, the same algorithm is applicable to each SACR profile with N range gates to determine the echo-free radar range gates. The output of the HS74 method is an estimate $P_n(\theta)$ of the received noise power, and it is used as a threshold to separate range gates into those with and without significant returns.

Several factors affect the value of $P_n(\theta)$. Millimeter-wavelength radar receiver noise has been shown to fluctuate as a function of environmental conditions and hardware component malfunctioning (Kollias et al. 2005). Atmospheric emission at millimeter wavelengths can also affect $P_n(\theta)$. Radars are effectively radiometers (Moore and Ulaby 1969) with excellent angular resolution but poor accuracy due to short integration times, narrow bandwidths, and poor antenna design. For example, the observed gradual increase in $P_n(\theta)$ at low elevation angles in Fig. 2 is due to enhanced atmospheric emission by gases—mainly water vapor. As expected, the observed radar receiver noise enhancement is higher at 94 GHz. In addition to emission by gases, the occurrence of liquid hydrometeors and melting particles in the radar beam further increases the SACR receiver noise due to emission by these hydrometeors. Thus, it is important to estimate the SACR radar receiver noise separately for each elevation angle; hence, the FM algorithm uses $P_n(\theta)$ as an ''emission enhanced'' reference noise power. While $P_n(\theta)$ is used to identify significant returns, it is not used in the estimation of the SACR radar reflectivity. The SACR radar reflectivity is estimated using internal, real-time noise power estimates produced by sampling directly receiver outputs for a short time period (comparable to the time that it takes to transmit two to three pulses) during every recorded profile when the radar is not transmitting pulses.

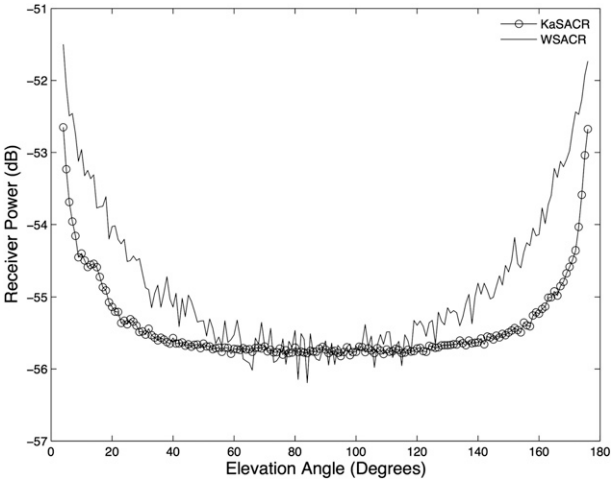

FIG. 2. SACR receiver mean noise power (with an arbitrary offset) as a function of elevation angle for the Ka band (gray line with small circles) and W band (black line). The data are from single horizon-to-horizon RHI scans for the two radar frequencies, and at each elevation the procedure described in section 2a is applied to estimate the mean receiver noise power at each elevation.

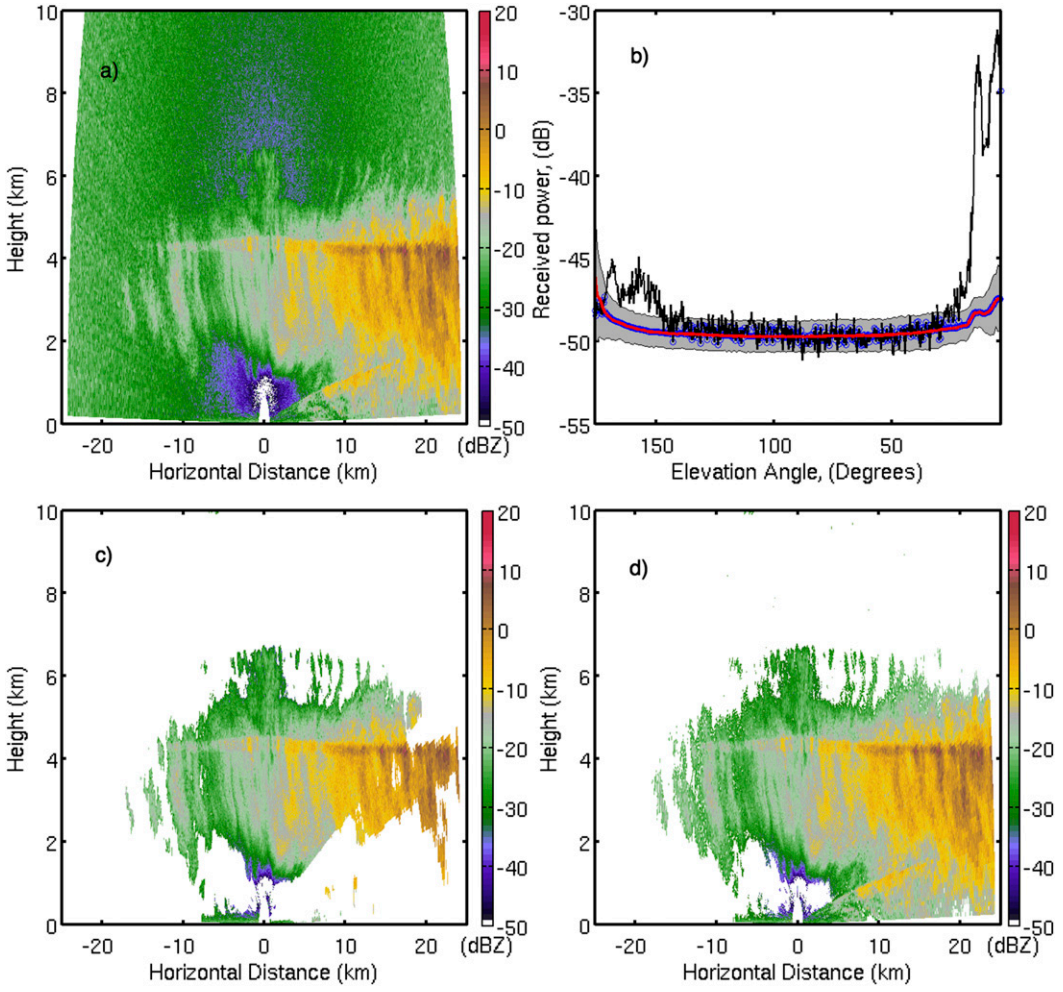

FIG. 3. (a) Raw Ka-SACR radar reflectivity measurements during a horizon-to-horizon RHI scan; (b) the Ka-SACR receiver noise estimated using HS74 (black line), the Ka-SACR receiver noise climatology mean (blue) plus and minus three standard deviations (gray), together with the adjusted Ka-SACR receiver noise power (red); (c) the Ka-SACR FM output using the HS74-estimated Ka-SACR receiver noise power [black line in (b)]; and (d) the Ka-SACR FM output using the adjusted Ka-SACR receiver noise power [red line in (b)].

Another factor that can substantially increase $P_n(\theta)$ occurs when atmospheric returns are present in all or a large portion of the recorded range gates (Fig. 3a). In this case, the HS74 algorithm does not have enough signal-free data points to produce an accurate estimate of $P_n(\theta)$, leading to highly inaccurate overestimates (Fig. 3b). This can lead to the misclassification of SACR atmospheric returns as hydrometeor-free range gates (Fig. 3c). To avoid this artifact, a ''climatologically derived'' estimate of the noise power obtained from a large collection of $P_n(\theta)$ values estimated from many consecutive RHI scans is used instead (Fig. 3d).

Using the recorded $P_n(\theta)$ at each θ, a first binary feature mask (FM1) along each radar profile (elevation angle) is produced. At each range gate i, the binary mask takes a value of 1 if $P_{rx}(i, \theta) \geq P_n(\theta)$ or a value of 0 if $P_{rx}(i, \theta) < P_n(\theta)$. The FM1$(i, \theta)$ binary mask is a reasonable indicator of the location of significant detections, though there are range gates with noisy powers higher than the threshold value. To eliminate these gates, a second two-dimensional mask is applied using a range–elevation angle filter. The two-dimensional filter is applied to 5×5 boxes of range gates (five consecutive range gates by five consecutive-in-elevation radar profiles) and counts the number of gates in the two-dimensional box [i.e., FM1$(i-2:i+2, \theta-2\Delta\theta:\theta+2\Delta\theta)$] that have values of 1. If this number is equal to or greater than 16, then the power return at the center of the 5×5 box is labeled as a significant return (i.e., 1) in the second and final feature mask, FM2(i, θ) (e.g.,

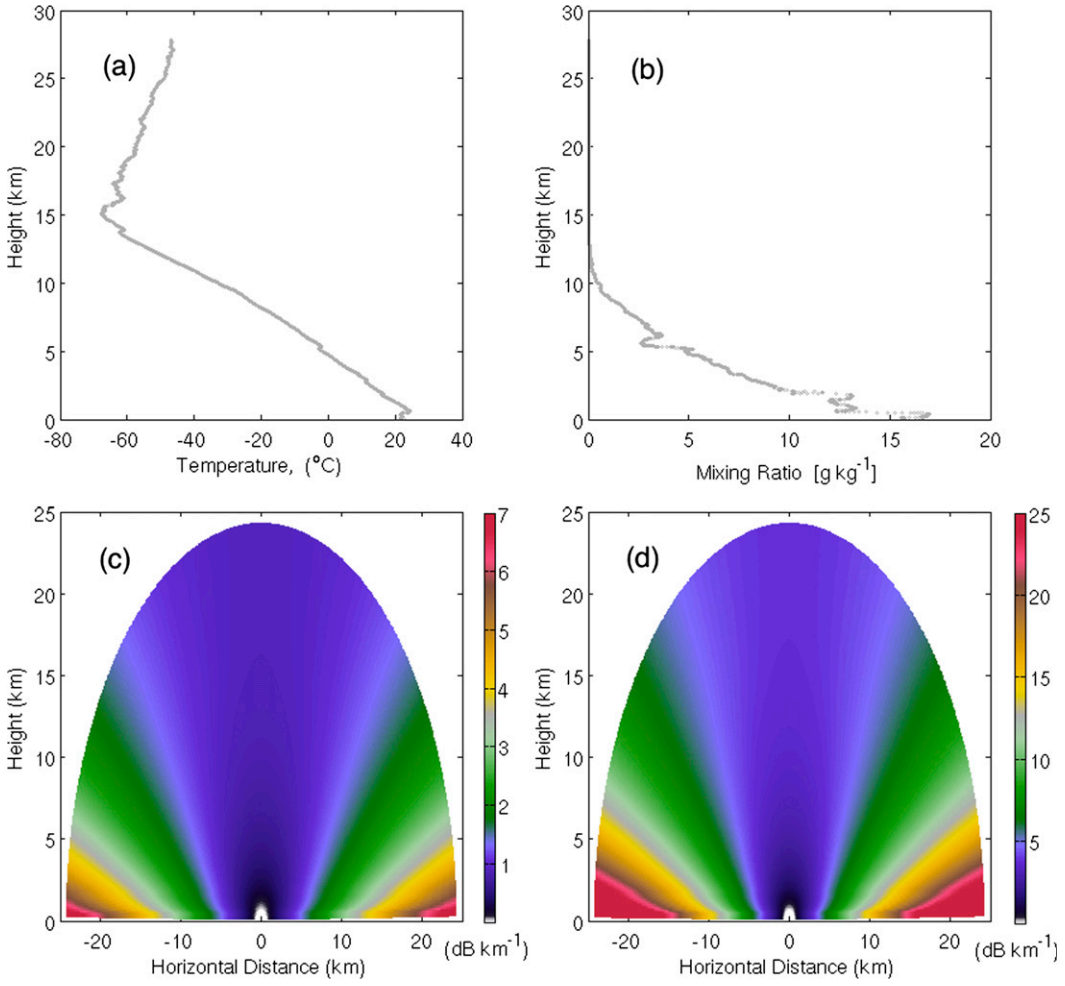

FIG. 4. (a) Temperature and (b) mixing ratio profiles from a sounding launched on 27 Jul 2012, during the ARM Mobile Facility deployment in Cape Cod; estimated two-way gaseous attenuation as a function of elevation angle and range for (c) Ka-SACR and (d) W-SACR.

Marchand et al. 2008; Clothiaux et al. 1995; Uttal et al. 1993). The range–elevation angle moving box is applied two or three times until all noisy gates are removed.

b. Water vapor attenuation correction

Absorption by atmospheric gases and hydrometeors limits the range and performance of millimeter-wavelength radars in precipitation and humid tropical and subtropical conditions (Lhermitte 1988; Clothiaux et al. 1995). This is especially true for scanning millimeter-wavelength radars at low elevation angles. For values of specific humidity as high as 20–25 g kg^{-1}, signal attenuation can reach 0.35 dB km^{-1} at 35 GHz and 2.0 dB km^{-1} at 94 GHz (Kollias et al. 2007). At each ARM fixed and mobile site, the balloon-borne sounding system (BBSS) provides the profile of temperature, pressure, and water vapor density every 6 h (Figs. 4a,b). The sounding data are assumed representative of the vertical structure of the atmosphere within a 30-km radius of the ARM sites. The temperature, pressure, and water vapor profiles are projected onto each SACR along-range profile. The line-by-line millimeter-wavelength propagation model developed by Liebe (1985) is used to estimate the attenuation coefficients k_{H_2O} and k_{O_2} in decibel per kilometer for water vapor and oxygen, respectively, for both the Ka and W bands (Figs. 4c,d). The observed radar reflectivity factor $Z_m(r)$ and the attenuation-corrected reflectivity factor $Z_e(r)$ are related through the relationship

$$Z_e(r) = \frac{Z_m(r)}{\exp\left[-0.2\ln(10)\int_0^r k_{H_20+O_2}(s)\,ds\right]}. \quad (1)$$

The reflectivity $Z_e(r)$ is corrected only for gaseous attenuation (Fig. 5). Attenuation due to hydrometeors is not corrected because this requires information on their water content amount and phase.

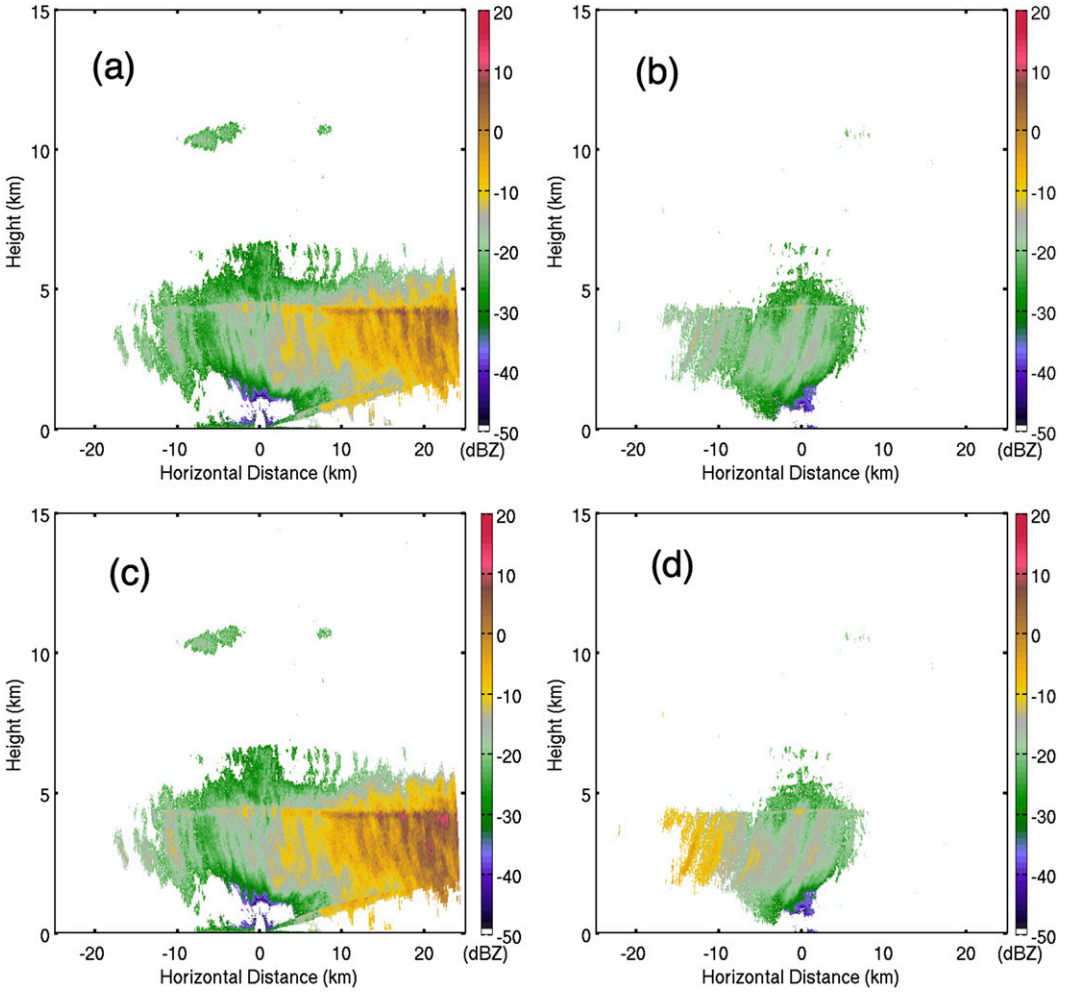

FIG. 5. (a) Raw Ka-SACR reflectivity and (b) raw W-SACR reflectivity recorded during the ARM Mobile Facility deployment to Cape Cod. The gaseous-attenuation-corrected (c) Ka-SACR and (d) W-SACR reflectivity fields. The Ka-SACR correction is small and thus difficult to spot; however, at the far-right positive range, it is possible to enhance reflectivity values in (c) in the melting layer and the rain layer below.

c. *Doppler velocity unfolding*

During scanning mode, both the Ka-band SACR (Ka-SACR) and W-band SACR (W-SACR) operate with a PRF of 5 kHz. This corresponds to Nyquist velocities V_N of ± 10.6 and $\pm 4\,\mathrm{m\,s^{-1}}$, respectively (Kollias et al. 2014). In the vertically pointing mode, the PRF used is higher and the corresponding higher Nyquist velocities result in limited aliasing that can be corrected using simple rules based on radar reflectivity thresholds and Doppler velocity continuity constraints. During scanning, the horizontal wind contribution to the observed Doppler velocity often results in multiple Doppler velocity foldings, especially when upper-tropospheric clouds are detected. Examples of observed Doppler velocity folding for the Ka-SACR and W-SACR are shown in Fig. 6. The influence of the horizontal wind on observed Doppler velocity is maximized at low elevation angles and minimized near zenith. The opposite is true for hydrometeor fall velocities. The combination of observed Doppler velocities from the Ka- and W-SACR can be used for generating unfolded Doppler velocities (Torres et al. 2004). However, the algorithm used here uses a single radar frequency to eliminate the necessity of both radar frequencies being operational.

First, the nearest (in time) sounding available at the ARM site is used to extract vertical profiles of the horizontal wind magnitude $V_H(z)$ and direction $\varphi_H(z)$. The horizontal wind profile is projected onto the plane scanned by the radar using the radar azimuth angle φ_{RHI} defined as follows:

$$V_{H,\mathrm{RHI}}(\theta, r) = V_H[z(\theta, r)]\cos\{\varphi_H[z(\theta, r)] - \varphi_{\mathrm{RHI}}\}, \quad (2)$$

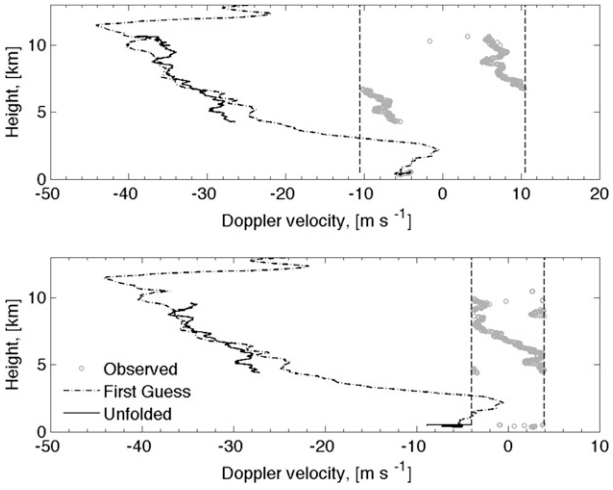

FIG. 6. Examples of Doppler velocity profiles corrected for folding for (a) Ka-SACR and (b) W-SACR observations. The observed Doppler velocity field is shown with circles, the first-guess Doppler velocity estimate based on the nearest sounding is shown with a dashed–dotted line, and the unfolded Doppler velocity is shown with the solid line. The vertical lines indicate the Nyquist velocity boundaries for the Ka-SACR and the W-SACR.

where $z(\theta, r)$ refers to a function that converts radar polar coordinates (r, θ) to height above the ground using the 4/3 Earth radius model for radar propagation (Doviak and Zrnić 1993). Examples of the first guess of the true Doppler velocity based on soundings are shown in Figs. 6 and 7b. At a particular θ and range r, the unfolded Doppler velocity $V_{\rm tr}$ is provided by the following expression:

$$V_{\rm tr}(\theta, r) = V_{H,\rm RHI}(\theta, r)\cos(\theta) + [V_T(\theta, r) + w_{\rm air}(\theta, r)]\sin(\theta), \quad (3)$$

where $V_{H,\rm RHI}$ is the horizontal wind projection on the (RHI) plane scanned by the radar, V_T is the reflectivity-weighted hydrometeor Doppler terminal velocity, $w_{\rm air}$ is the vertical air motion (assuming positive Doppler velocity toward the radar), and θ is taken between 0° and 90°. The SACR, at θ and r, observes a Doppler velocity V_D provided by the following equation:

$$V_D(\theta, r) = V_{\rm tr}(\theta, r) + F(\theta, r)2V_N, \quad (4)$$

where $F(\theta, r)$ is the matrix that contains the number of velocity folds at each observation point in the scanned plane. Thus, unfolding of the SACR Doppler velocities requires estimation of $F(\theta, r)$. To a first approximation, the contribution of the second term on the right side of Eq. (5) is neglected and thus a first estimate of the unfolded Doppler velocity $V_{\rm tr}^{\rm est}$ is provided by $V_{\rm tr}^{\rm est}(\theta, r) \approx V_{H,\rm RHI}(\theta, r)\cos(\theta)$. Subsequently, a first estimate of $F^{\rm est}(\theta, r)$ is provided by

$$F^{\rm est}(\theta, r) = \text{round}\left[\frac{V_{\rm tr}^{\rm est}(\theta, r) - V_D(\theta, r)}{2V_N}\right]. \quad (5)$$

An example of $F^{\rm est}(\theta, r)$ for a Ka-SACR horizon-to-horizon RHI scan is shown in Fig. 7c. The first estimate of $F^{\rm est}(\theta, r)$ is used to estimate the unfolded Doppler velocity using Eq. (6) (Figs. 6a, 7d). The unfolded Doppler velocity field is finally evaluated for sharp velocity discontinuities within each hydrometeor layer. This is accomplished using a Doppler velocity continuity (smoothness) constraint from one SACR range gate to the next, assuming that the unfolded Doppler velocity at the top of each hydrometeor layer is correct. This algorithm has been tested on more than one year of SACR Doppler velocity observations. The Doppler velocity-unfolding algorithm performs well in more than 98% of cases. In the future, the single-frequency-based Doppler unfolding algorithm will be evaluated using coincident observed Doppler velocity measurements from both SACR frequencies.

d. Filtering of insect contributions to radar returns

The presence of insect radar echoes (''atmospheric plankton''; Lhermitte 1966) in the boundary layer can limit our ability to properly define hydrometeor-layer boundaries and locations. Insects are mainly an issue during the summer months at the Southern Great Plains (SGP) ARM site in Oklahoma, where small insects produce strong radar echoes in the lowest 2–3 km of the atmosphere (Clothiaux et al. 2000; Luke et al. 2008; Chandra et al. 2013). Insects have radar reflectivities comparable to those from typical boundary layer clouds. Several techniques have been proposed to identify radar returns contaminated by insects. Martner and Moran (2001) reported that the use of polarimetric radar measurements augmented with information about the cloud-base height from a lidar was helpful in identifying the presence of insect contributions to the measurements. Multifrequency radar observations at the ARM SGP site have demonstrated that dual-wavelength ratio (DWR) measurements at 35- and 94-GHz (SACR) frequencies and linear depolarization ratio (LDR) measurements can be used for identifying insects in a cloudy boundary layer (Sekelsky et al. 1998; Khandwalla et al. 2001). More recently, Luke et al. (2008) suggested the use of radar Doppler spectra–based techniques for the automatic identification of insects in the radar sample volume.

Currently, the SACRs record Doppler spectra only when pointing vertically (Kollias et al. 2014). Here, only single-radar frequency approaches to insect filtering are discussed to enhance the operational robustness of the

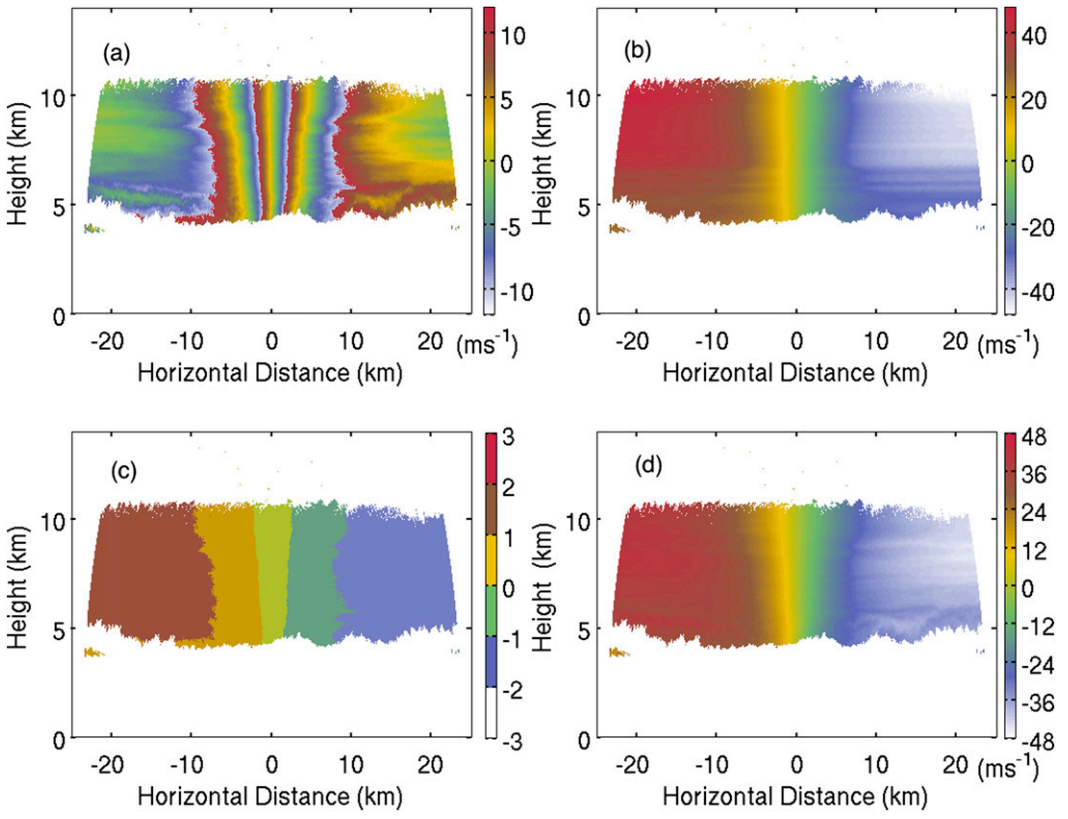

FIG. 7. (a) Ka-SACR Doppler velocity field during a horizon-to-horizon RHI scan, (b) the first-guess Ka-SACR Doppler velocity field, (c) the number of foldings, and (d) the unfolded Doppler velocity field.

algorithm and to avoid the constraint for both radars to be operational all the time. During vertical profiling observations, the recorded radar Doppler spectra, combined with LDR measurements, ceilometer cloud-base heights, and temperature profiles, will be used to discriminate insects (Luke et al. 2008). During scanning observations, no radar Doppler spectra are available and insect filtering will be based primarily on LDR measurements. Figure 8a shows an example of Ka-SACR LDR observations during a horizon-to-horizon RHI scan at the ARM SGP site. The observations show a shallow precipitating cloud at ranges +10 to +20 with LDR values clustered around −35 dB. These low values of LDR are a product of the high copolar precipitation returns and the SACR antenna cross-polarization isolation, which is around −35 dB. Three shallow, nonprecipitating cumuli clouds at ranges −10 to −8, −5 to −3 km, and over the SACR location are also observed with LDR values around −20 dB. The LDR values in these clouds are determined only by the strength of their copolar return (their cross-polarization signal generated by the antenna is below the receiver noise). Finally, insects in the lowest 2 km are responsible for the high LDR values. Using all Ka-SACR LDR measurements collected during the summer of 2011 at the ARM SGP site during all sky conditions in the lowest 3 km of the atmosphere as a function of elevation angle is shown in Fig. 8b. The dataset contributing to Fig. 8b includes a large number of horizon-to-horizon scans with insects, shallow nonprecipitating cumuli, and precipitating shallow clouds. In general, insects are characterized by high LDR values (e.g., the right peak in the LDR frequency of occurrence distribution in Fig. 8b). Liquid cloud droplet LDR returns are determined by the strength of the copolar return, and the LDR of small raindrops is determined by the SACR antenna cross-polarization isolation. The low LDR values, which are very high-elevation angles, are produced when the precipitating system passes over the SACR location.

The insect-filtering algorithm is applied only to Ka-SACR returns at heights with temperatures higher than 5°C. According to Luke et al. 2008, insects are rarely found in temperatures colder than 10°C. If there are significant radar detections at temperatures warmer than 5°C, then the next step is to use the ceilometer cloud-base height detections within a 1-h window around the time of interest. If there are no cloud-base height detections in the lowest 3 km within the 1-h window (this

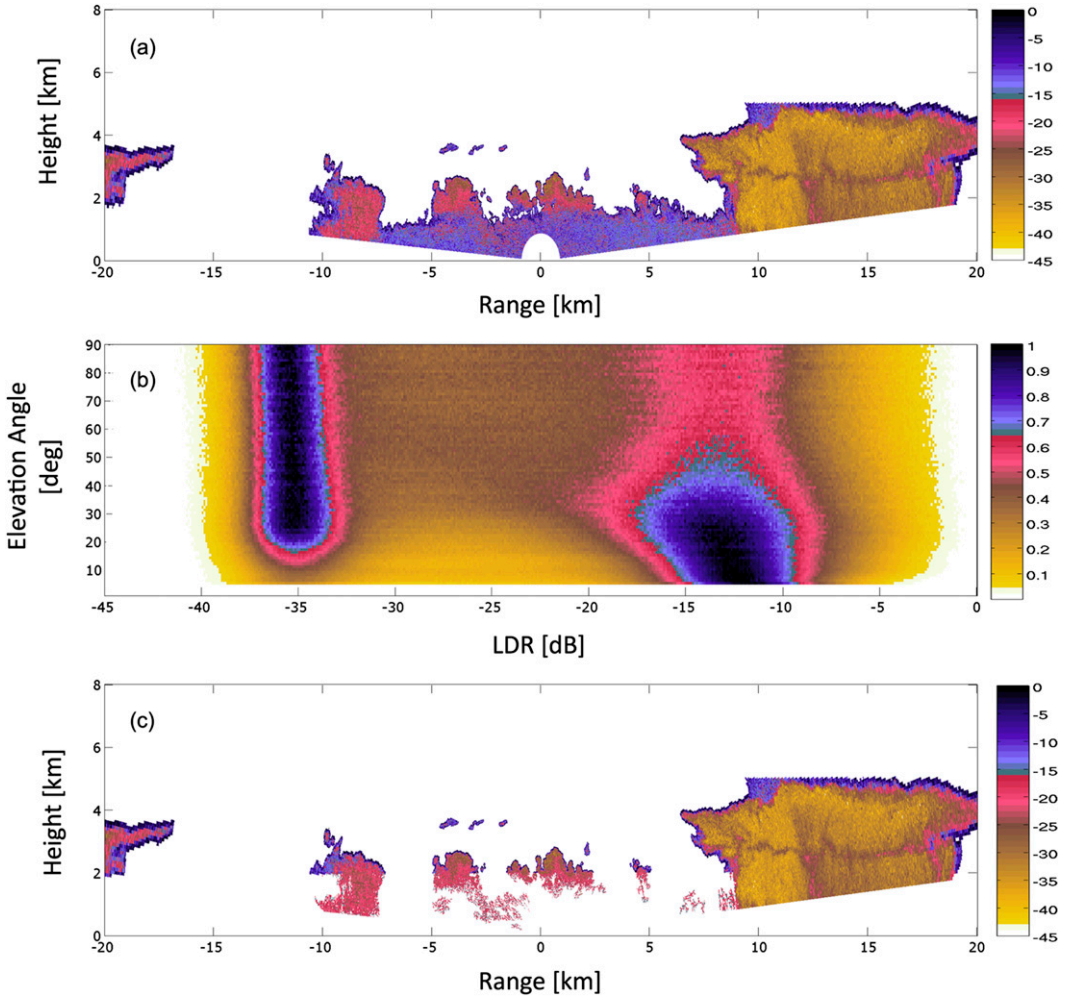

FIG. 8. (a) Example of Ka-SACR LDR observations during summertime at the ARM SGP site. The melting layer is around 3 km. Shallow cumuli, insects, and shallow precipitating clouds are observed. (b) Distribution of Ka-SACR LDR values observed at the ARM SGP site as a function of elevation angle. (c) Example of Ka-SACR LDR observations (as in Fig. 8a) filtered for insect returns.

situation is frequently encountered during the summertime over the SGP site), then all low-level SACR detections are flagged as insects. If the ceilometer detects cloud bases in the lowest 3 km within the 1-h window, then the average cloud-base height is used to constrain the maximum height to which the insect-filtering algorithm is applied. An LDR threshold value of -15 dB is initially used to conservatively distinguish insect (LDR > -15) and hydrometeor returns (LDR ≤ -15). A two-dimensional filtering mask, similar to the one applied for the FM, is then applied to remove remaining insect-contaminated radar returns. Figure 8c illustrates the performance of the proposed insect filtering on the raw data shown in Fig. 8a. Our ability to distinguish clouds from insects is limited near the cloud edges. In the future, the algorithm will be continuously evaluated and improved using coincident DWR and LDR measurements at 35- and 94-GHz frequencies when available.

3. Horizontal wind retrievals using HS-RHI observations

During the HS-RHI scan strategy, the radar samples the atmosphere from horizon to horizon at six different azimuth angles evenly spaced apart by 30°. The radar first performs the north–south scan, rotates 30° counterclockwise and scans the atmosphere in the south-southeast–north-northwest direction, rotates again 30° counterclockwise and performs the west-northwest–east-southeast scan, and then the east–west scan is performed and after two more such rotations the HS scan is

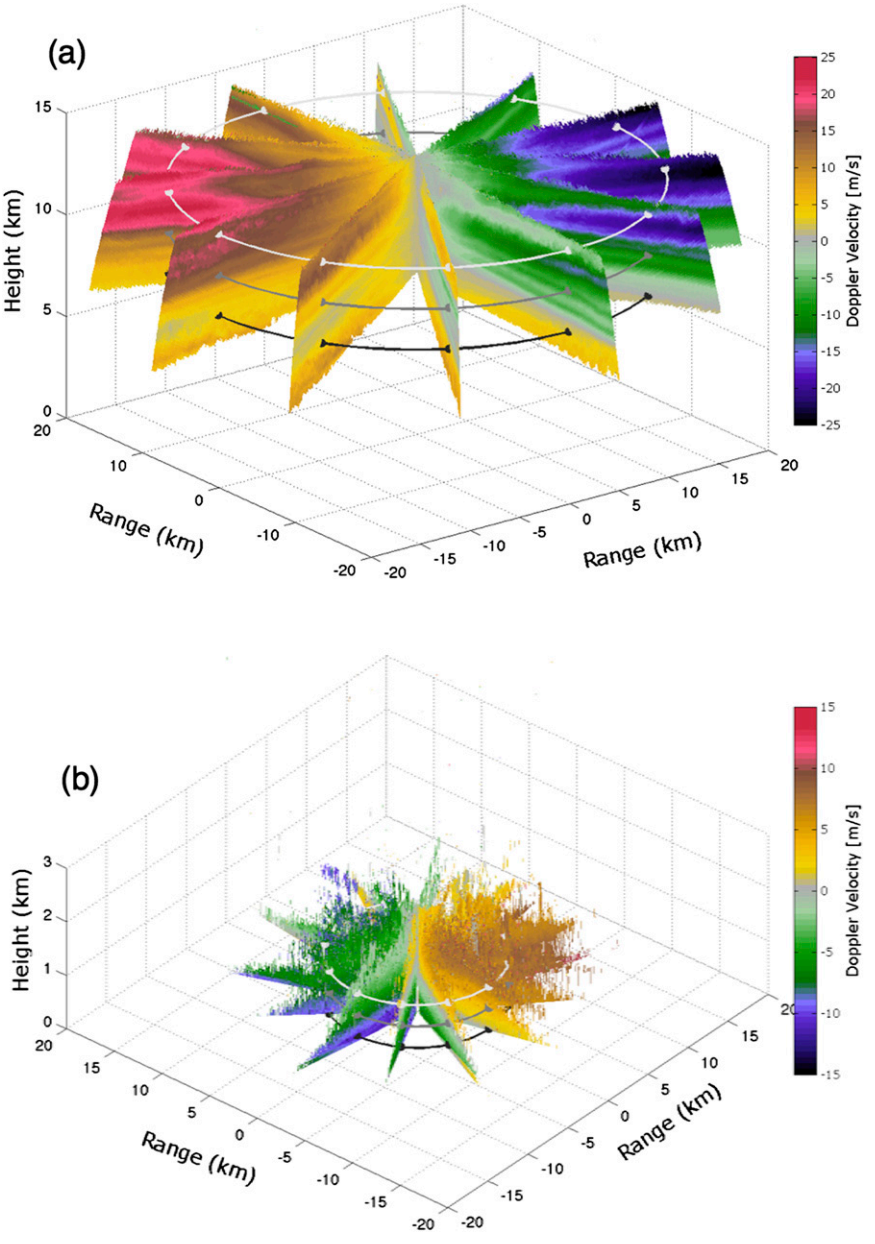

FIG. 9. Example observations of unfolded Ka-SACR mean Doppler velocities obtained from two sets of HS-RHI scans—one occurring when (a) cirrus clouds were present and the other during a period when (b) insects dominated the returns in the boundary layer.

complete. It takes about 35 s to perform one horizon-to-horizon scan and less than 3 min to complete one complete HS-RHI scan (Kollias et al. 2014).

Two examples of unfolded Doppler velocity measurements mapped on the planes sampled in a HS-RHI set of scans are shown in Fig. 9. The first example is from a cirrus cloud layer (Fig. 9a), and the second example contains low-level insect-contaminated radar returns (Fig. 9b). At each height, a maximum of 12 (two for each of the six planes in the scan) Ka-SACR Doppler velocity measurements are available for the horizontal wind velocity retrievals (in case of overcast cloud or insect conditions). These horizontal wind velocities are retrieved using the velocity–azimuth display (VAD) technique (e.g., Lhermitte and Atlas 1961; Browning and Wexler 1968; Rabin and Zrnić 1980; Siemen and Holt 2000; Gao et al. 2004). Because the SACR samples the cloud field at all elevations, an elevation angle between

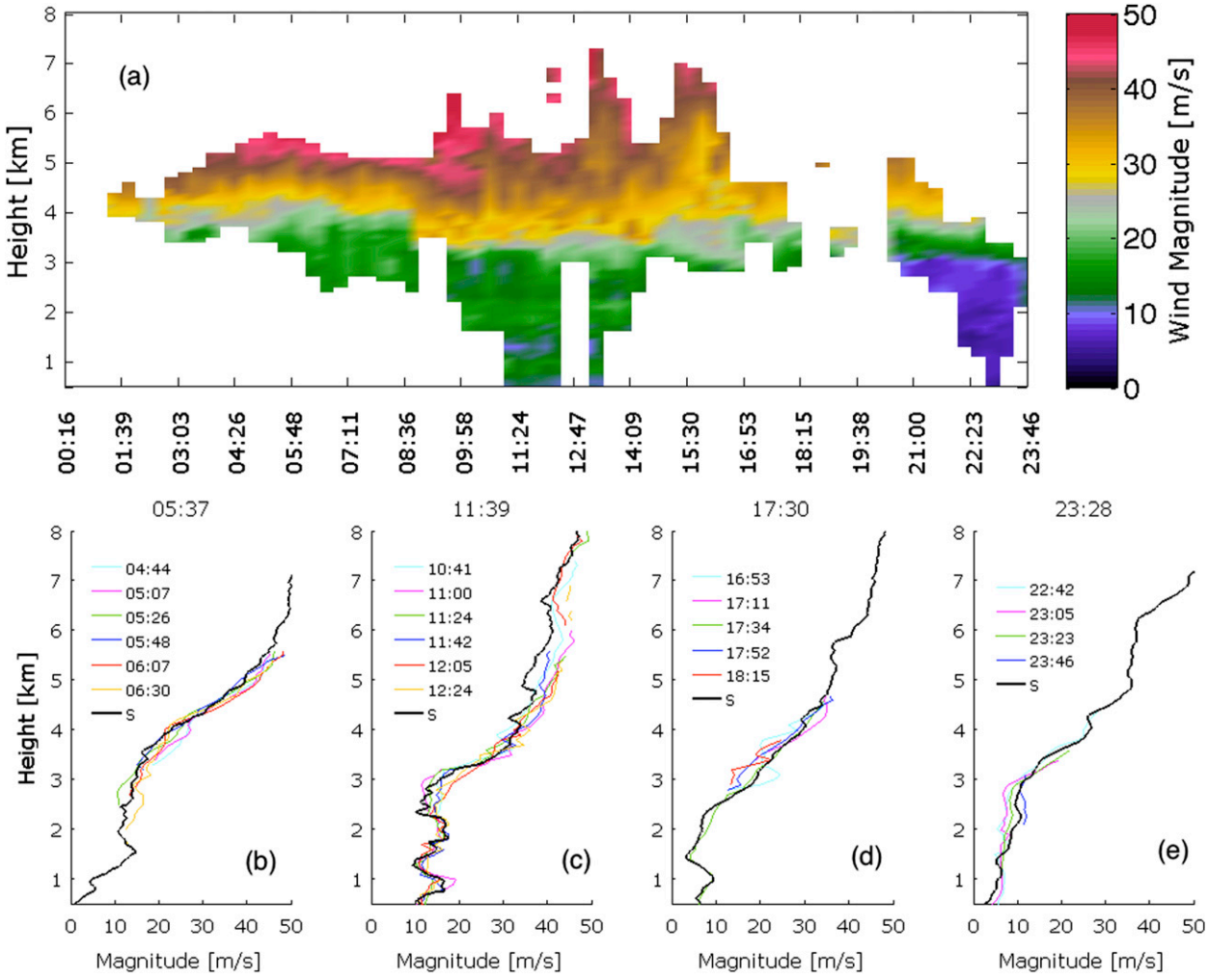

FIG. 10. (a) Diurnal evolution of the retrieved wind magnitude at heights where cloud and/or precipitation was detected by the SWACR on 1 May 2010. (b)–(e) Wind magnitude profiles from the four SGP soundings (black lines) and wind magnitude profiles retrieved by the VAD technique applied to the HS-RHI scan measurements within a 3-h window centered on the sounding times (color lines). The time (UTC) of each sounding is indicated at the top of each plot, and the times of each HS-RHI set of scans used in a retrieval are indicated by the color lines with time labels in the legends.

60° and 75° (represented by the circles and solid dots in Fig. 9) is used in the retrievals, resulting in a small sampling volume. The technique can also be applied in cases where the cloud conditions are not overcast at a particular height, and the number of possible wind retrievals is therefore less than 12.

Two 24-h periods with scanning cloud radar observations in the ARM SGP site are used to demonstrate the application of the VAD technique. The first case consists of a total of 69 HS-RHI sets of scans performed by the scanning W-band ARM cloud radar (SWACR) during a 24-h observing period on 1 May 2010. The SWACR was the first ARM scanning cloud radar deployed, prior to the installation of the SACRs. On 1 May a thick midlevel cloud layer that produced precipitation at the ground is observed (Fig. 10a). The diurnal evolution of the retrieved horizontal wind velocity magnitudes at heights where hydrometeors are detected is shown. The wind velocity magnitudes increased with height throughout the entire atmospheric layer analyzed, with the only exception occurring from 1000 to 1400 UTC, when decreases in horizontal wind speed with height are noticeable in the layer below 3 km (Fig. 10a). The retrieved horizontal wind directions present sharp gradients in height in the first 3 km of the atmosphere, where the retrieved wind direction changes from southwesterly (in the lowest levels) to westerlies (around 2 km) and then back to southwesterly (Fig. 11a).

The second case was observed by the Ka-SACR on 1 June 2011 (Fig. 12a). No hydrometeors were observed;

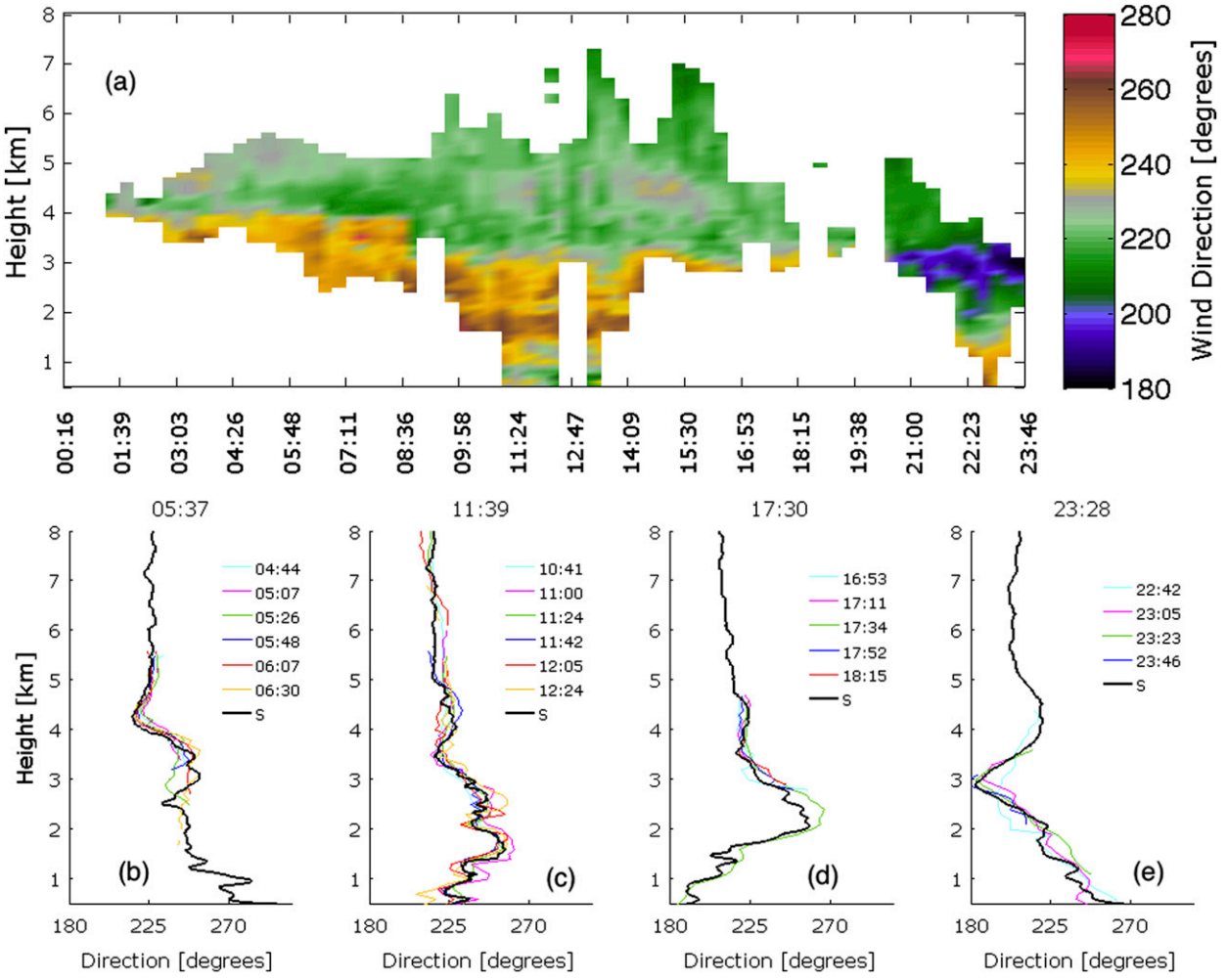

FIG. 11. (a) Diurnal evolution of the retrieved wind direction at heights where cloud and/or precipitation was detected by the SWACR on 1 May 2010; (b)–(e) wind direction profiles from the four SGP soundings (black lines) and wind direction profiles retrieved by the VAD technique applied to the the HS-RHI scan measurements within a 3-hwindow centered on the sounding times (color lines). The time (UTC) of each sounding is indicated at the top of each plot, and the times of each HS-RHI set of scans used in a retrieval are indicated by the color lines with time labels in the legends.

however, the horizontal wind retrieval was performed in the boundary layer using SACR Doppler velocity measurements from insects (Luke et al. 2008). Not surprisingly, large variability in the diurnal evolution of the retrieved horizontal wind speed profile is observed (Fig. 12a), whereas a clear veering profile is noticeable during this day from 0000 to 0700 UTC, from northeasterly winds in the lower levels to strong southerlies at the top of the boundary layer (Fig. 13a). During the morning hours, the horizontal wind weakens and the wind direction becomes more stable with height (Figs. 12a, 13a). The wind speed increases from 1100 UTC to the end of the analyzed period, reaching values of 15 m s^{-1} around 1400 UTC, whereas the wind direction presents a remarkably sustained southerly component through the entire boundary layer. In this case, the wind retrievals were performed as part of a scan sequence that included other scan strategies (Kollias et al. 2014). As a result, the wind retrieval for this day has a lower temporal resolution than for the previous example, with a total of 40 HS-RHI scans for the 24-h period.

The four soundings launched daily at the ARM SGP site provide an independent source of horizontal wind profiles that can be used to compare with the performance of the HS-RHI-based retrievals (Figs. 10–13). During the 1 May 2010 case, the wind magnitude and direction comparisons show very good agreement (Figs. 10, 11). The root-mean-square (rms) errors between the sounding and the retrieved horizontal wind profiles within a 3-h window centered on the sounding times are

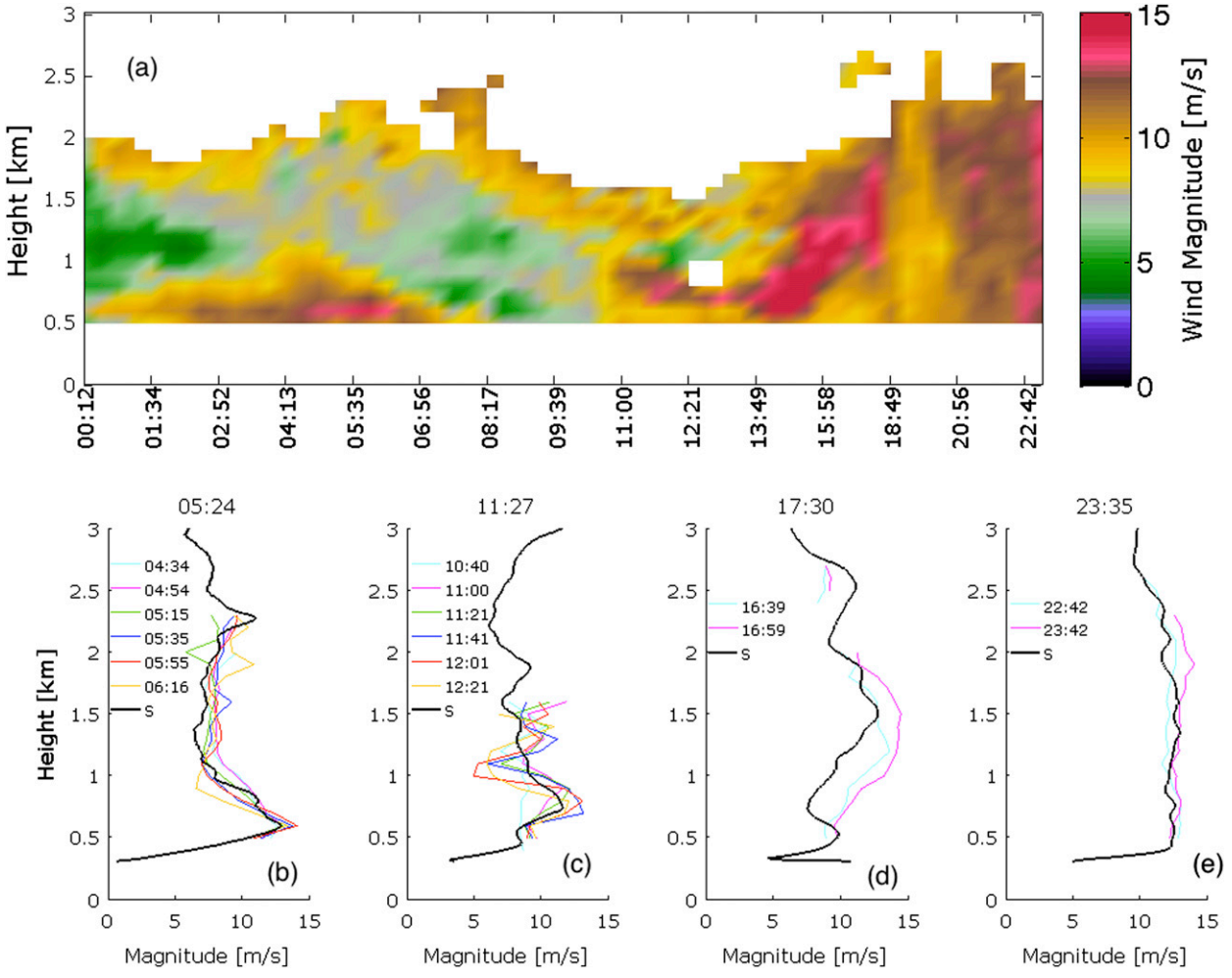

FIG. 12. (a) Diurnal evolution of the retrieved wind magnitude in heights where insects were detected by the SACR on 1 Jun 2011. (b)–(e) Wind magnitude profile from the four SGP soundings (black lines) and wind magnitude profile retrieved by the HS-RHI within a 3-h window around the sounding time (color lines). The time of the sounding is indicated in the title of each plot, and the HS-RHI time is also labeled on each plot.

2.3, 2.7, 2.3, and 1.8 m s^{-1} for the wind magnitude and 11.2°, 6.4°, 8.2°, and 13.8° for the wind direction. The large-scale features of the horizontal wind retrieved by the HS-RHI observations agree very well with those observed with the soundings. This is especially the case in the lowest 3 km of the atmosphere for the 1139 UTC sounding, where the variations in the wind speeds and directions are well captured by the retrieved horizontal wind (Figs. 10, 11).

The comparison between the retrieved and measured horizontal wind profiles is poorer in the insect case. This could be attributed to the high spatial variability of the insect field and the strong vertical velocity motions in the boundary layer. Nonetheless, the correspondence between the observed and retrieved wind magnitude is exceptional. The rms errors between the sounding and the retrieved horizontal wind profiles within a 3-h window centered on the sounding times are 1.5, 3.9, 2.1, and 1.0 m s^{-1} for the wind magnitude and 7.6°, 14.2°, 7.2°, and 5.0° for the wind direction. For example, the sharp gradient present in wind speed from 0.4 to 1 km in the 0054 and 1127 UTC soundings is well captured by the retrieved wind (Fig. 12). However, the retrieved wind speeds at later sounding times seem to have a higher variability in the vertical than observed in the sounding measurements (Fig. 12). With respect to the horizontal wind directions during this day, the retrieved and measured profiles also agree very well, with the exception of the morning and noon soundings (1127 and 1730 UTC), when the retrieved wind directions do present some discrepancies from the observed wind directions, particularly around 1 km (Fig. 13).

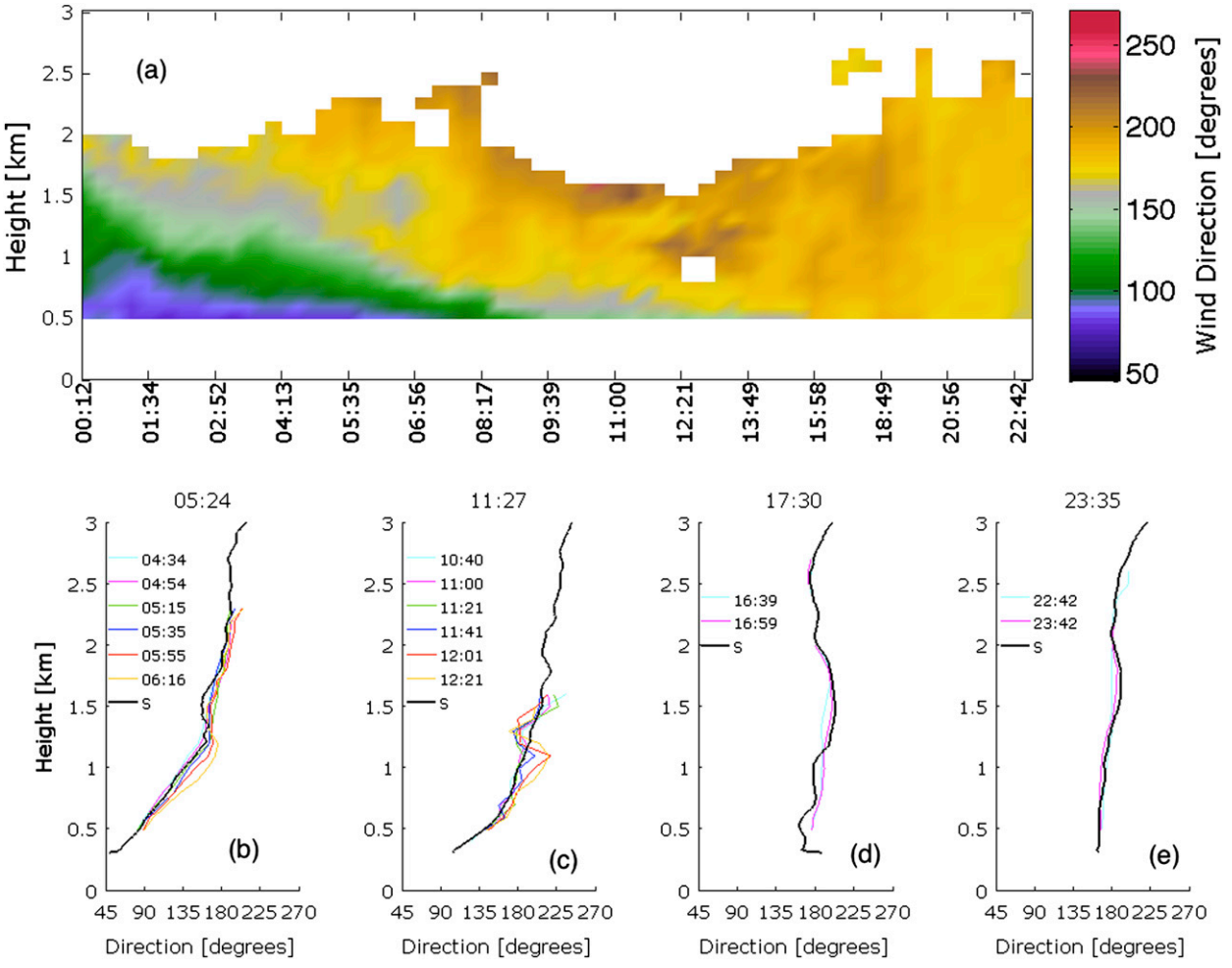

FIG. 13. (a) Diurnal evolution of the retrieved wind direction in heights where insects were detected by the SACR on 1 Jun 2011. (b)–(e) Wind direction profile from the four SGP soundings (black lines) and wind direction profile retrieved by the HS-RHI within a 3-h window around the sounding time (color lines). The time of the sounding is indicated in the title of each plot, and the HS-RHI time is also labeled on each plot.

4. Summary

ARM operates dual-frequency scanning, polarimetric Doppler cloud radars (SACRs) at all its fixed and mobile sites (Kollias et al. 2014). The data from the SACRs are going to be large in volume, multiparametric, and in need of substantial postprocessing to have their value fully realized by the atmospheric research community. The first level of postprocessing of the SACR raw observations is described here. The postprocessed SACR observables are expected to provide a first view of the three-dimensional cloud structure around the ARM sites. More importantly perhaps, the postprocessed SACR observables will be the starting point for the development of higher-order products, including gridded three-dimensional hydrometeor locations, dynamical and turbulence products, and single- and dual-frequency-based retrievals of microphysical parameters of interest to the scientific community.

The first step in SACR data postprocessing is the determination of the FM. The FM algorithm identifies the SACR range gates that contain atmospheric returns, including nonmeteorological targets (e.g., insects) and second-trip echoes. The most important step in the FM algorithm is the objective determination of the SACR receiver noise. For each SACR profile, this is accomplished using the HS74 algorithm. A two-dimensional binary mask is subsequently applied to the initial results produced by the HS74 algorithm to improve the FM. The output of the FM algorithm is used for determination of the hydrometeor fraction and of the number of hydrometeor layers and associated base and top heights using radar-only observations.

The nearest (in time) atmospheric sounding is used to provide information on the profiles of water vapor, pressure, and temperature. The information from the sounding along with standard atmospheric O_2 concentration is projected to the SACR slant path at each elevation angle. The slanted projections are used as input into the Liebe (1985) line-by-line absorption model to estimate the two-way gaseous attenuation along all SACR propagation paths. The attenuation is applied to the observed SACR reflectivity measurements.

The unfolding of the SACR Doppler velocity radar observations is another part of postprocessing. The horizontal wind velocity magnitudes and directions from the nearest atmospheric sounding are used to provide an initial estimate of the radial Doppler velocity that would be observed by the SACR at each elevation angle in the absence of velocity folding. The estimated radial Doppler velocity field and the SACR Nyquist velocity are used to develop a first guess of the number of velocity foldings. The first guess, the FM output, and observed Doppler velocity field are used to find the along-range SACR Doppler velocity solution that minimizes the velocity differences between the solution and the initial estimate.

Finally, the output of the FM, the Ka-SACR radar reflectivity, and LDR measurements, along with the temperature profile and the ceilometer cloud-base statistics within a 2-h time window centered on the SACR observations, are used as input into the insect-filtering algorithm.

As is customary with operational products, several improvements and refinements will be added to the proposed algorithms and data products as more observations are available from the ARM fixed and mobile sites. Furthermore, it is conceivable that dual-wavelength measurements of radar reflectivity and Doppler velocity will be used in the future to validate and improve the presented algorithms. These algorithms are based on single-frequency measurements in order to increase the robustness of their application to all single-frequency Ka- and W-SACR data streams.

Finally, the presented algorithms address the challenge of SACR data quality control. The SACR quality-controlled observations have already been used to develop 3D gridded cloud products (Lamer et al. 2013), to study the temporal evolution of clouds (Borque et al. 2013, manuscript submitted to *J. Appl. Meteor. Climatol.*), and to improve microphysical retrievals (Tridon et al. 2013). While these efforts improve our understanding of how to use the SACR observations, the more general questions raised in the introduction are more complex, and input from the broader community is needed to adequately address them. The existing limitations in the SACR scan capabilities (see Kollias et al. 2014, Part I) clearly eliminate the possibility of volume imaging the entire cloudy atmosphere in acceptable time resolution; thus, we need to be clever on how to best sample the cloudy atmosphere in three dimensions. The HS-RHI scan is expected to provide initial information on the 3D cloud field structure in discrete directions, and this is a good first step forward compared to the time–height curtain mapping of clouds provided by the profiling facilities. The zeroth-order information that the SACRs should obtain is 3D cloud locations and this, in return affects the way we sample the atmosphere. The SACR sensitivity loss with range affects our ability to map objectively 3D cloud structure, since we always "detect" more clouds near the SACR location. Information from ground-based total-sky imagers, ceilometers and scanning microwave and infrared radiometers, and high-resolution satellite images should be eventually merged to provide a best estimate of the 3D cloudy atmospheric state.

Acknowledgments. We would like to acknowledge the effort of the ARM infrastructure at all the fixed and mobile sites that contributed in the deployment and operation of the SACR systems. The U.S. DOE Atmospheric Radiation Measurement program funded the presented research.

REFERENCES

Browning, K. A., and R. Wexler, 1968: The determination of kinematic properties of a wind field using Doppler radar. *J. Appl. Meteor.,* **7,** 105–113.

Chandra, A., P. Kollias, and B. Albrecht, 2013: Multiyear summertime observations of daytime fair-weather cumuli at the ARM Southern Great Plains Facility. *J. Climate,* **26,** 10 031–10 050.

Clothiaux, E. E., M. A. Miller, B. A. Albrecht, T. A. Ackerman, J. Verlinde, D. M. Babb, R. M. Peters, and W. J. Syrett, 1995: An evaluation of a 94-GHz radar for remote sensing of cloud properties. *J. Atmos. Oceanic Technol.,* **12,** 201–229.

——, T. P. Ackerman, G. G. Mace, K. P. Moran, R. T. Marchand, M. A. Miller, and B. E. Martner, 2000: Objective determination of cloud heights and radar reflectivities using a combination of active remote sensors at the ARM CART sites. *J. Appl. Meteor.,* **39,** 645–665.

Doviak, R. J., and D. S. Zrnić, 1993: *Doppler Radar and Weather Observations.* 2nd ed. Academic Press, 562 pp.

Gao, J., K. K. Droegemeier, J. Gong, and Q. Xu, 2004: A method for retrieving mean horizontal wind profiles from single-Doppler radar observations contaminated by aliasing. *Mon. Wea. Rev.,* **132,** 1399–1409.

Hildebrand, P. H., and R. S. Sekhon, 1974: Objective determination of the noise level in Doppler spectra. *J. Appl. Meteor.,* **13,** 808–811.

Khandwalla, A., S. M. Sekelsky, L. Li, and M. Bergada, 2001: Theory and observations between Ka-band and W-band to explain scattering differences between insects. *Proc. 11th ARM*

Science Team Meeting, Atlanta, GA, DOE ARM, 5 pp. [Available online at http://www.arm.gov/publications/proceedings/conf11/extended_abs/khandwalla_a.pdf.]

Kollias, P., B. A. Albrecht, E. E. Clothiaux, M. A. Miller, K. L. Johnson, and K. P. Moran, 2005: The Atmospheric Radiation Measurement Program cloud profiling radars: An evaluation of signal processing and sampling strategies. *J. Atmos. Oceanic Technol.,* **22,** 930–948.

——, E. E. Clothiaux, M. A. Miller, B. A. Albrecht, G. L. Stephens, and T. P. Ackerman, 2007: Millimeter-wavelength radars: New frontier in atmospheric cloud and precipitation research. *Bull. Amer. Meteor. Soc.,* **88,** 1608–1624.

——, N. Bharadwaj, K. Widener, I. Jo, and K. Johnson, 2014: Scanning ARM cloud radars. Part I: Operational sampling strategies. *J. Atmos. Oceanic Technology,* in press.

Lamer, K., A. Tatarevic, I. Jo, and P. Kollias, 2013: Evaluation of gridded Scanning ARM Cloud Radar reflectivity observations and vertical Doppler velocity retrievals. *Atmos. Meas. Tech. Discuss.,* **6,** 9579–9621, doi:10.5194/amtd-6-9579-2013.

Lhermitte, R. M., 1966: Probing air motion by Doppler analysis of radar clear air returns. *J. Atmos. Sci.,* **23,** 575–591.

——, 1988: Cloud and precipitation remote sensing at 94-GHz. *IEEE Trans. Geosci. Remote Sens.,* **26,** 207–216.

——, and D. Atlas, 1961: Precipitation motion by pulse Doppler radar. *Proc. Ninth Weather Radar Conf.,* Boston, MA, Amer. Meteor. Soc., 218–223.

Liebe, H. J., 1985: An updated model for millimeter wave propagation in moist air. *Radio Sci.,* **20,** 1069–1089, doi:10.1029/RS020i005p01069.

Luke, E. P., P. Kollias, K. L. Johnson, and E. E. Clothiaux, 2008: A technique for the automatic detection of insect clutter in cloud radar returns. *J. Atmos. Oceanic Technol.,* **25,** 1498–1513.

Marchand, R., G. G. Mace, T. Ackerman, and G. Stephens, 2008: Hydrometeor detection using *Cloudsat*—An earth-orbiting 94-GHz cloud radar. *J. Atmos. Oceanic Technol.,* **25,** 519–533.

Martner, B. E., and K. P. Moran, 2001: Using cloud radar polarization measurements to evaluate stratus cloud and insect echoes. *J. Geophys. Res.,* **106** (D5), 4891–4897.

Moore, R. K., and F. T. Ulaby, 1969: The radar radiometer. *Proc. IEEE,* **57,** 587–590.

Moran, K. P., B. E. Martner, M. J. Post, R. A. Kropfli, D. C. Welsh, and K. B. Widener, 1998: An unattended cloud-profiling radar for use in climate research. *Bull. Amer. Meteor. Soc.,* **79,** 443–455.

Rabin, R. M., and D. S. Zrnić, 1980: Subsynoptic-scale vertical wind revealed by dual Doppler-radar and VAD analysis. *J. Atmos. Sci.,* **37,** 644–654.

Sekelsky, S. M., and Coauthors, 1998: Comparison of millimeter-wave cloud radar measurements for the fall 1997 cloud IOP. *Proc. Eighth ARM Science Team Meeting,* Tucson, AZ, DOE ARM, 5 pp. [Available online at http://www.arm.gov/publications/proceedings/conf08/extended_abs/sekelsky_sm.pdf.]

Siemen, S., and A. R. Holt, 2000: A modified VAD technique for analysing wind fields with Doppler radar. *Phys. Chem. Earth,* **25B,** 1201–1204.

Torres, S. M., Y. F. Dubel, and D. S. Zrnić, 2004: Design, implementation, and demonstration of a staggered PRT algorithm for the WSR-88D. *J. Atmos. Oceanic Technol.,* **21,** 1389–1399.

Tridon, F., A. Battaglia, and P. Kollias, 2013a: Disentangling Mie and attenuation effects in rain using a K_a-W dual-wavelength Doppler spectral ratio technique. *Geophys. Res. Lett.,* **40,** 5548–5552, doi:10.1002/2013GL057454.

Uttal, T., L. I. Church, B. E. Martner, and J. S. Gibson, 1993: CLDSTATS: A cloud boundary detection algorithm for vertically pointing radar data. NOAA Tech. Memo. ERL WPL-233, 28 pp.